

Wright State University

CORE Scholar

[Browse all Theses and Dissertations](#)

[Theses and Dissertations](#)

2012

Dielectric Constant Measurements Using Atomic Force Microscopy System

Hembathanthirige Yasas Dhanapala
Wright State University

Follow this and additional works at: https://corescholar.libraries.wright.edu/etd_all



Part of the [Physics Commons](#)

Repository Citation

Dhanapala, Hembathanthirige Yasas, "Dielectric Constant Measurements Using Atomic Force Microscopy System" (2012). *Browse all Theses and Dissertations*. 1101.
https://corescholar.libraries.wright.edu/etd_all/1101

This Thesis is brought to you for free and open access by the Theses and Dissertations at CORE Scholar. It has been accepted for inclusion in Browse all Theses and Dissertations by an authorized administrator of CORE Scholar. For more information, please contact library-corescholar@wright.edu.

DIELECTRIC CONSTANT MEASUREMENTS USING ATOMIC FORCE MICROSCOPY SYSTEM

A thesis submitted in partial fulfillment
of the requirements for the degree of
Master of Science

By

YASAS DHANAPALA

B.S., Wittenberg University, 2009

2012

Wright State University

Wright State University
SCHOOL OF GRADUATE STUDIES

August 23, 2012

I HEREBY RECOMMEND THAT THE THESIS PREPARED UNDER MY
SUPERVISION BY Hembathanthirige Yasas Dhanapala ENTITLED Dielectric
Constant Measurement Using Atomic Force Microscopy System BE
ACCEPTED IN PARTIAL FULFILLMENT OF THE REQUIREMENTS FOR THE
DEGREE OF Master of Science.

Gregory Kozlowski, Ph.D.
Thesis Director

Douglas Petkie, Ph.D.
Chair, Department of Physics

Committee on
Final Examination

Gary Farlow, Ph.D.

Ivan Medvedev, Ph.D.

Gregory Kozlowski, Ph.D.

Andrew Hsu, Ph.D.
Dean, Graduate School

ABSTRACT

Dhanapala, Yasas. M.S., Department of Physics, Wright State University, 2012
Dielectric Constant Measurement Using Atomic Force Microscopy System

A new technique to obtain local dielectric constant of thin films was developed using atomic force microscopy system. This technique, in addition to other characterization methods such as AFM imaging and X-Ray diffraction, was used to study, as an example, dielectric constant of thin films of $0.3\text{BiScO}_3 - 0.7\text{BaTiO}_3$. The thin films were fabricated by using pulsed laser deposition technique under following temperature of the substrate: 650°C , 700°C and 750°C . At each temperature, two different oxygen pressures were used in deposition chamber: 50 mTorr and 100 mTorr. Our goal was to find optimal growth conditions with the highest dielectric constant and compare it with their structural properties. In addition, our dielectric constant calculations were generalized to include a wider range of film thicknesses.

Contents

1	Introduction	1
2	Materials	11
2.1	Thin Film Fabrication Process	12
2.1.1	Deposition Process.....	13
2.1.2	Growth Conditions	17
3	Material Characterization	18
3.1	X-Ray Diffraction	18
3.2	Atomic Force Microscopy	20
3.2.1	AFM imaging	22
4	Measurement of Dielectric Constant Using AFM	26
4.1	Theoretical Background	26
4.2	Parameter Calibration.....	32
4.2.1	Spring Constant.....	32
4.2.2	Surface Voltage	33
4.2.3	Cone Angle	34
4.2.4	Tip Radius.....	35
4.2.5	Stray Deflection.....	35
4.3	Procedure.....	36
4.3.1	Sample Preparation	36
4.3.2	Measurement Protocol.....	37
5	Results.....	39
5.1	Atomic Force Microscopy	39
5.2	X-Ray Diffraction	42
5.3	Dielectric Constants	44
6	Discussion and Conclusions	48
7	Bibliography	52

List of Figures

FIGURE 1.1. PARALLEL PLATE CAPACITOR.	2
FIGURE 1.2. LOSS TANGENT VECTOR DIAGRAM.	3
FIGURE 1.3. FREQUENCY RESPONSE OF DIELECTRIC MECHANISMS.	4
FIGURE 1.4. DIPOLE ROTATION IN ELECTRIC FIELD.	5
FIGURE 1.5. FREE SPACE MEASUREMENT SETUPS.	8
FIGURE 2.1. A DIAGRAM OF THE PLD CHAMBER USED FOR THIN FILM GROWTH.	14
FIGURE 3.1. DIAGRAM OF BRAGG'S LAW.	19
FIGURE 3.2. 228MM LONG MICRO-FABRICATED SILICON CANTILEVER WITH INTEGRATED TIP.	21
FIGURE 3.3. NANOSURF EASYSKAN 2 CONTROLLER WITH THE AFM SCAN HEAD.	23
FIGURE 4.1. DIELECTRIC MEASUREMENT SET-UP OF THIN FILM SAMPLE DEPOSITED ON A SUBSTRATE WITH A CONDUCTIVE LAYER. A DC VOLTAGE BIAS IS APPLIED BETWEEN THE SUBSTRATE AND THE CANTILEVER. THE RESULTING DEFLECTION D DEPENDS ON THE LOCAL DIELECTRIC CONSTANT OF THE SAMPLE.	26
FIGURE 4.2. CROSS SECTION OF THE SAMPLE AFTER ETCHING SHOWING AN ETCH DEPTH OF 330 NM.	36
FIGURE 4.3. SAMPLE PREPARED FOR MEASUREMENT WITH GROUNDED CREATED BY USING SILVER PAINT DROP.	37
FIGURE 5.1. 5MM \times 5MM COLOR MAP OF BSBT SAMPLE #3505.	39
FIGURE 5.2. LINE PROFILES (B) FOR BSBT SAMPLE # 3505 (A).	40
FIGURE 5.3. INTENSITY VERSUS 2θ ANGLE FOR BSBT SAMPLE (# 3505) WITH GAUSSIAN FIT.	42
FIGURE 5.4. DEFLECTION VERSUS Z DISTANCE WITH EQUATION 4.17 FITTED FROM $Z = 100$ NM TO $Z = 30$ NM ABOVE THE METALLIC BUFFER LAYER.	45

FIGURE 5.5. DEFLECTION VERSUS VOLTAGE FOR SAMPLE # 3501 MEASURED 100 NM ABOVE THE SAMPLE

AT COORDINATES (2.05,-1.05). 46

FIGURE 5.6. DEFLECTION VERSUS Z DISTANCE WITH THE AVERAGE TAKEN AROUND 180 NM ABOVE THE

SAMPLE # 3501. 47

List of Tables

TABLE 1.1. STATIC RELATIVE PERMITTIVITY.....	6
TABLE 1.2. SUMMARY OF THE MEASUREMENT TECHNIQUES (MUT STANDS FOR MATERIAL UNDER TEST AND μ_r IS RELATIVE PERMEABILITY).....	7
TABLE 2.1. THIN FILMS GROWN WITH DEPOSITION PARAMETERS.	17
TABLE 3.1. ANSCM-PT CANTILEVER SPECIFICATIONS.	25
TABLE 5.1. COLOR MAPS OF BSBT THIN FILMS DEPOSITED AT DIFFERENT TEMPERATURES AND TWO PARTIAL OXYGEN PRESSURES (100 MTORR, A) AND (50 MTORR, B), RESPECTIVELY TOGETHER WITH AVERAGE ROUGHNESS.	41
TABLE 5.2. INTENSITY VERSUS 2θ FOR EACH SAMPLE. HERE PEAKS 1, 2 AND 3 REPRESENTS BSBT(200), SRO(200) AND LSAT(200), RESPECTIVELY. PEAK # 1 OF EACH SAMPLE IS FITTED WITH A GAUSSIAN CURVE.....	43
TABLE 5.3. GRAIN SIZES CALCULATED FROM BSBT(200) X-RAY DIFFRACTION PEAK.	44
5.4. DEFLECTION, STRAY DEFLECTION, SURFACE VOLTAGE, EQUILIBRIUM POSITION AND THE DIELECTRIC CONSTANT CALCULATED FOR EACH BSBT SAMPLE.	47
TABLE 6.1. SUMMARY OF FABRICATION CONDITIONS, GRAINS SIZES, ROUGHNESS VALUES AND RELATIVE DIELECTRIC CONSTANTS FOR THE SIX BSBT SAMPLES.	50

Acknowledgement

First I would like to extend my thanks to my academic advisor Dr. Gregory Kozlowski who guided, educated and helped me throughout my Master's degree. I would also like to acknowledge the time he spent helping with my thesis as well as time spent providing me with the thin film samples. I would also like to thank Dr. Gregory Kozlowski as well as Dr. Gary Farlow and Dr. Ivan Medvedev for sitting on my committee.

I would like to thank Wright State University for their support in my pursuance of this degree. Additionally, I would like to extend my thanks to Dr. Steven Higgins for helping me overcome the technical issues I encountered with the equipment used in this study.

In addition, I would like to mention my colleagues Zafrullah Jagoo and Anna Lukawaska for the help and support they extended towards me.

My gratitude also goes out to my family for the encouragement and the motivation they provided throughout this project and all my other accomplishments.

1 Introduction

Permittivity is a property which describes how much electrical charge a material can store in a given volume or a measure of the material's property of slowing electromagnetic waves down. It controls also the value of a capacitor beyond its physical dimensions. The units of permittivity are Farads/meter (F/m) and its value denoted by ϵ_0 is equal to 8.8542×10^{-12} F/m in free space. Materials have permittivity $\epsilon_{\text{material}}$ higher than ϵ_0 and their dielectric properties are characterized by relative permittivity or dielectric constant $\epsilon_r = \epsilon_{\text{material}}/\epsilon_0$.

The dielectric constant ϵ_r of a material under given conditions reflects the extent to which it concentrates electrostatic lines of flux. In technical terms, it is the ratio of the amount of electrical energy stored in a material by an applied voltage relative to that stored in a free space. Likewise, it is also the ratio of the capacitance of a capacitor using that material as a dielectric, compared to a similar capacitor that has a free space as its dielectric. A material is classified as dielectric if it has the ability to store energy when an external electric field is applied. If a DC voltage source is placed across a parallel plate capacitor, more charge is stored when a dielectric material is between the plates than if no material (a vacuum) is between the plates. The dielectric material increases the storage capacity of the capacitor by neutralizing charges at the electrodes, which

ordinarily would contribute to the external field. The capacitance with the dielectric material is related to the dielectric constant. If a DC voltage source V is placed across a parallel plate capacitor, more charge is stored when a dielectric material is between the plates than if no material (a vacuum) is between the plates. The capacitance of parallel plate capacitor depicted in Figure 1.1 is expressed by

$$C = C_0 \epsilon_r = (\epsilon_r \epsilon_0 A) / t \quad (1.1)$$

where C and C_0 are capacitance with and without dielectric, ϵ_r is relative permittivity or real dielectric constant, and A and t are the area of the capacitor plates and the distance between them, respectively.

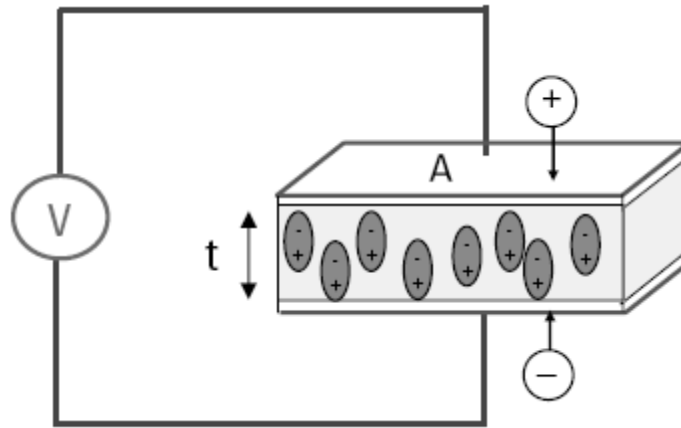


Figure 1.1. Parallel plate capacitor.

The dielectric material increases the storage capacity of the capacitor by neutralizing charges at the electrodes, which ordinarily would contribute to the external field. From the point of view of electromagnetic theory, permittivity describes the interaction of a material with an electric field E and is a complex number (Equation 1.2):

$$\epsilon_r = \epsilon'_r - i\epsilon''_r \quad (1.2)$$

The real part of permittivity ϵ'_r is a measure of how much energy from an electric field is stored in a material. The imaginary part of permittivity ϵ''_r is called the loss factor and is a measure of how dissipative or lossy a material is to an external electric field. The imaginary part of permittivity ϵ''_r is always greater than zero and is usually much smaller than ϵ'_r . The loss vector includes the effects of both dielectric loss and conductivity ($\epsilon''_r = \epsilon''_{dr} + \sigma/\omega\epsilon_0$ for lossy material such as a metal). When complex permittivity is drawn as a simple vector diagram (Figure 1.2), the real and imaginary components are 90° out of phase.

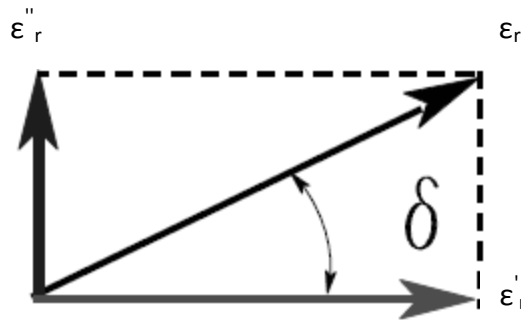


Figure 1.2. Loss tangent vector diagram.

The relative lossiness of a material is the ratio of the energy lost to the energy stored (Equation 1.3).

$$\tan\delta = \left[\frac{(\epsilon_r)''}{\epsilon'_r} \right] = D = \frac{1}{Q} = \frac{\text{energy lost}}{\text{energy stored}} \quad (1.3)$$

where D and Q are dissipation and quality factor, respectively. A material may have several dielectric mechanisms that contribute to its overall permittivity (Figure 1.3). A dielectric

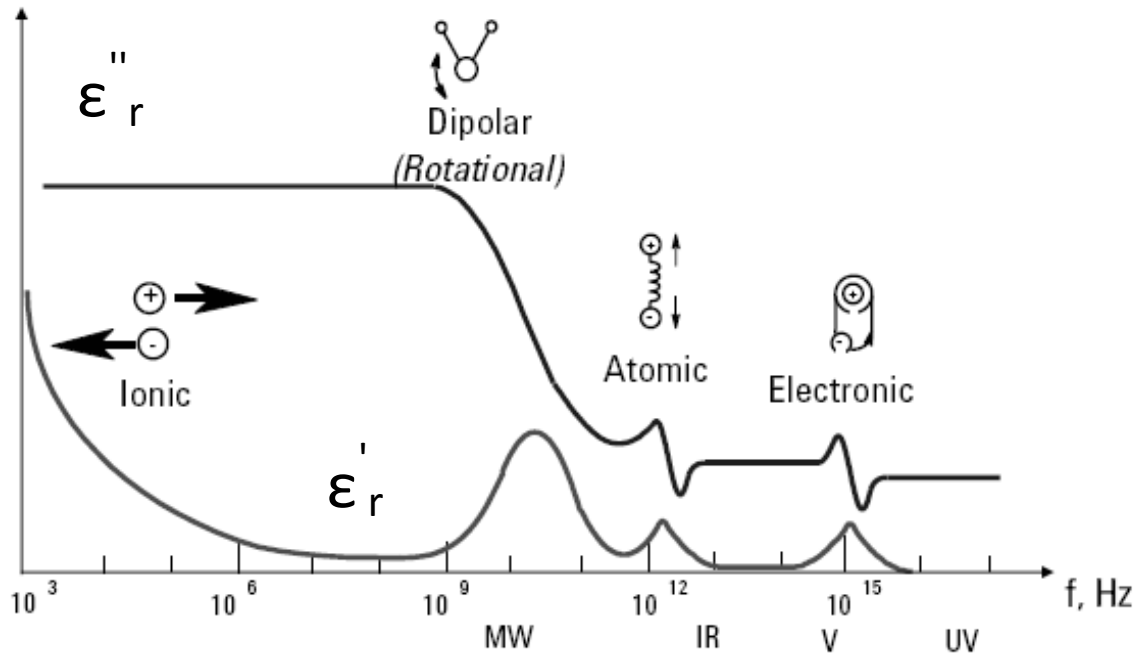


Figure 1.3. Frequency response of dielectric mechanisms.

material has an arrangement of electric charge carriers that can be displaced by an electric field. Dipole orientation or polarization together with ionic conduction mechanism contributes to permittivity significantly in the range of frequency from DC to microwave. Dipolar polarization appears when rearrangement of electrons in a formation process of molecules may cause an imbalance in charge distribution creating a permanent dipole moment. The electric field E will rotate the dipole due to presence of torque τ causing orientation polarization to occur (Figure 1.4).

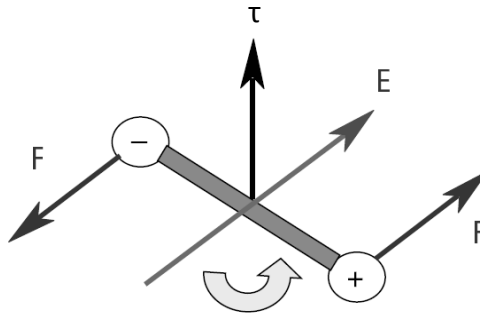


Figure 1.4. Dipole rotation in electric field.

The friction accompanying the orientation of the dipole will contribute to the dielectric losses. The dipole rotation causes a variation in both ϵ'_r and ϵ''_r . Electronic polarization occurs in neutral atoms when an electric field displaces the nucleus with respect to the electrons that surround it. Atomic polarization occurs when adjacent positive and negative ions stretch under an applied electric field. The electronic and atomic mechanisms contribute only a small constant amount to ϵ'_r and are almost lossless far below resonance. A peak of maximum absorption in ϵ''_r appears at resonance frequency and, finally, the contribution from these mechanisms disappears above the resonance. In this study, we will concentrate only on the real part of the dielectric constant. The imaginary part of the dielectric constant, or absorption, approaches zero when the frequency of the external field reaches zero. Since the technique described in Chapter 4 occurs under a DC bias we can safely neglect it. Relative static permittivity of some materials at room temperature under 1 kHz frequency is presented in Table 1.1.

Material	ϵ'_r
Vacuum	1.00
Polypropylene	2.36
Carbon disulfide	2.60
Paper	3.85
Silicon dioxide	3.90
Concrete	4.50
Pyrex	4.70
Rubber	7.00
Diamond	5.50
Graphite	10.00
Silicon	11.68
Ethylene Glycol	37.00
Glycerol	41.20
Water	80.10
Sulfuric acid	92.00
Titanium dioxide	130.00
Strontium titanate	310.00
Barium strontium titanate	500.00
Barium titanate	1250–10,000
Lead zirconate titanate	500–6000
Calcium copper titanate	>250,000

Table 1.1. Static relative permittivity.

There are several experimental techniques to measure permittivity. The most commonly used are: coaxial probe, transmission line, free space method, resonant cavity and very simple method of parallel plate mentioned before. Many factors such as accuracy, convenience, and the material shape and form are important in selecting the most appropriate measurement technique. Some of the significant factors to consider are summarized in Table 1.2.


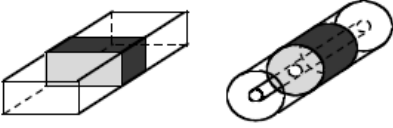
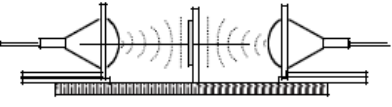
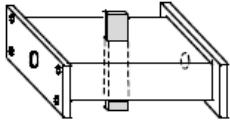
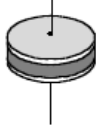
Coaxial probe ϵ_r		Broadband, convenient, non-destructive Best for lossy MUTs; liquids or semi-solids
Transmission line ϵ_r and μ_r		Broadband Best for lossy to low loss MUTs; machineable solids
Free space ϵ_r and μ_r		Non-contacting Best for high temperatures; large, flat samples
Resonant cavity ϵ_r and μ_r		Accurate Best for low loss MUTs; small samples
Parallel plate ϵ_r		Accurate Best for low frequencies; thin, flat sheets

Table 1.2. Summary of the measurement techniques (MUT stands for Material Under Test and μ_r is relative permeability).

The open-ended coaxial probe is cut off section of transmission line. The material is measured by immersing the probe into a liquid or touching it to the flat face of a solid material. The field at the probe end “fringe” into the material and change as they come into contact with the sample. The reflected signal S_{11} can be measured and related to ϵ_r . Transmission line methods involve placing the material inside a portion of an enclosed transmission line. The line is usually a section of rectangular waveguide or coaxial airline. ϵ_r is computed from the measurement of the reflected signal S_{11} and transmitted signal S_{21} . Free-space method use antenna to focus microwave energy at or through a

slab of material. Figure 1.5 shows two typical free-space measurement setups: an S-parameter configuration and reflect line arch arrangement.

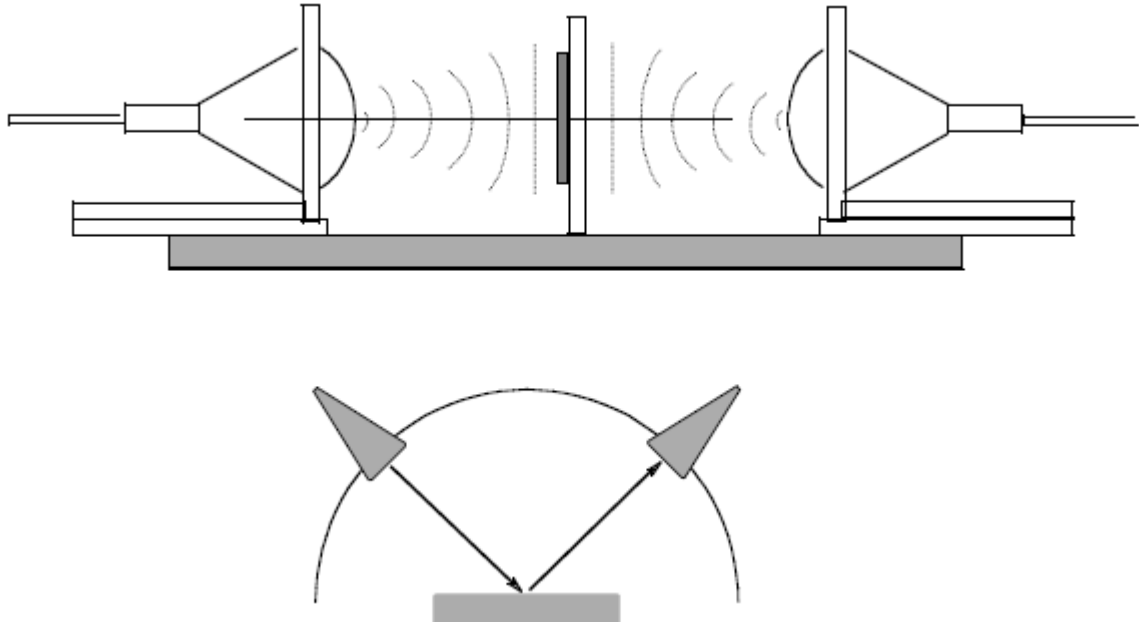


Figure 1.5. Free space measurement setups.

Resonant cavities are high Q structures that resonate at certain frequencies. A piece of sample affects frequency and quality factor of the cavity. From these parameters, the complex permittivity of the material can be calculated at a single frequency. The parallel plate capacitor method involves sandwiching a thin sheet of material between two electrodes to form a capacitor. A typical measurement system using the parallel plate method consists of an LCR meter or impedance analyzer and a fixture such as the 16451B dielectric test fixture, which operates up to 30 MHz.

A number of techniques to measure local dielectric properties of thin films, based on scanning probe microscopy have been developed over recent years. Most of these methods utilize scanning force microscopy (SFM), a sub-category of scanning

probe microscopy, to study electrostatic and dielectric properties of thin films [1, 2, 3, 4, 5]. These techniques are based on detecting the capacitive force or the current flowing through a conductive probe with a nano- sized tip. The topography of sample along with the dielectric properties of the material at a nano-scale spatial resolution can be obtained. However, these techniques can be complex and difficult due to the long-range nature of the electrical interaction and the complications raised by the tip geometry. In order to obtain the dielectric parameters of the materials there is a need to use approximated analytical models and/or numerical solutions [6].

As a solution to the above-mentioned problem, a simple analytical model has been developed to quantify accurately a tip-sample capacitance of thin dielectric films [7]. This model has been used in several studies and has yielded successful results. In one of the studies local capacitance measurements have been obtained with a current sensing nano-scale capacitance microscope [8, 9]. The above mentioned model [7] has also been used to successfully quantify the low frequency dielectric constant of thin SiO_2 films [10]. The dielectric constants of supported bio-membranes have been measured in a similar fashion in [11]. However, these studies have utilized extremely sensitive instrumentation (sub-attofarad capacitance resolution) for current sensed dielectric microscopy.

My main aim of the study has been to develop a localized on nano-scale dielectric constant or DC relative permittivity measurement of $(0.3)\text{BiScO}_3$ -(0.7) BaTiO_3 epitaxial and dielectric thin films by using a commercially available atomic force

microscope [6]. In this study, I will obtain quantitative dielectric constants of these films which were fabricated by using pulsed laser ablation deposition system under different deposition conditions as far as a partial pressure of oxygen and substrate temperature are concerned. In addition, I will examine the composition and the morphology of the films by using XRD and AFM imaging technique respectively and compare the results with their dielectric properties.

Chapter 2 of my thesis discusses the procedure used in fabrication of the materials as well as the growth conditions used during their depositions. XRD measurement and AFM imaging used to study the composition and the morphology of the materials are explained in Chapter 3. In Chapter 4, I take an in-depth look at the measurement of the dielectric constant, ϵ_r . This Chapter will include the theoretical background of the technique and measurement protocol used in the calculation of ϵ_r . Chapter 5 summarizes the results obtained by using techniques described in Chapter 4. Lastly, in Chapter 6, I will discuss the results and draw conclusions for identifying the optimized conditions in the fabrication process in order to obtain the best quality film with the highest dielectric constant.

2 Materials

As an application of the technique developed to examine thin films, we measured a set of thin films with a similar composition but fabricated under different deposition conditions such as a partial oxygen pressure and substrate temperature. In this Chapter, we will discuss the significance of the materials being tested.

High permittivity dielectrics are useful both in capacitor applications and in piezoelectrics since the piezoelectric coefficient is proportional to the dielectric constant of a well-poled material. Currently, the capacitor industry makes extensive use of BaTiO_3 as a high permittivity dielectric material. Despite the high dielectric value in bulk form, thin films of BaTiO_3 display a radically low permittivity, especially, when the film thickness is in the nanometer regime. However, lead-based materials such as $\text{PbZr}_{1-x}\text{Ti}_x\text{O}_3$ (PZT) retain higher permittivities in thin film form.

The material under my investigation, $x\text{BiScO}_3-(1-x)\text{BaTiO}_3$ (BSBT), has been identified as a lead-free alternative which facilitate the retention of high permittivity at small dielectric thicknesses. Thin films of $x\text{BiScO}_3-(1-x)\text{BaTiO}_3$ with x ranging from 0.2 to 0.6 has been investigated in [12]. Here BSBT dielectric films were fabricated on a $\langle 100 \rangle$ LaAlO_3 single layer crystal substrates along with a SrRuO_3 electrode. Results found in [12] displayed permittivities reaching up to 800 for $(0.4)\text{BiScO}_3-(0.6)\text{BaTiO}_3$ composition.

With an analogous objective in mind we investigate $(0.3)\text{BiScO}_3\text{--}(0.7)\text{BaTiO}_3$ deposited on a $\langle 100 \rangle$ $\text{LaAlO}_3\text{Sr}_2\text{AlTaO}_6$ (LSAT) single crystal substrate instead of LaAlO_3 . The choice of alternate substrate was made to circumvent complications raised in the fabrication process as described in the following section.

2.1 Thin Film Fabrication Process

The thin films were fabricated using Pulsed Laser Deposition (PLD). Precise control of the deposition parameters is important in this process because even a small change in the deposition parameters would drastically alter the orientation of the final product [13].

The samples were prepared by growing $(0.3)\text{BiScO}_3\text{--}(0.7)\text{BaTiO}_3$ (BSBT) dielectric films and SrRuO_3 buffer layers (electrode) on a $\langle 100 \rangle$ LSAT substrate by using PLD for 50 mTorr and 100 mTorr partial pressure of oxygen and for substrate temperature of 650°C , 700°C and 750°C . LaAlO_3 (LAO) substrate used in [12] had a drawback because of creation of the spontaneous strain in films associated with cubic–rhombohedral phase transition of the substrate at elevated temperature. Lanthanum aluminate is rhombohedral at room temperature. However, at temperature around 600°C , LaAlO_3 undergoes a phase transition from rhombohedral to cubic [14]. The pulsed laser deposition process, described in the next section, requires the substrate initially to be at even higher temperature than structural transition temperature. This causes the substrate to change from cubic to rhombohedral structure when cooling down after the

PLD process is completed. This change exerts strain on the BSBT thin films causing them to crack.

2.1.1 Deposition Process

Pulsed laser deposition (PLD) as a versatile technique in many aspects, was first used by Smith and Turner in 1965 for the preparation of semiconductor and dielectric thin films. With this method, thin films are prepared by the ablation of one or more targets illuminated by a focused pulsed laser beam. Since the energy source is located outside the chamber, the use of ultra-high vacuum as well as ambient gas is possible. Combined with a stoichiometry transfer between target and substrate this allows depositing wide range of different materials. The pulsed nature of the process also allows fabricating complex polymer-metal compounds and multilayers. In UHV, implantation and intermixing effects originating in the deposition of energetic particles lead to the formation of metastable phases, for instance nanocrystalline highly supersaturated solid solutions and amorphous alloys. Fabrication in inert gas atmosphere makes it even possible to control film properties such as stress, texture, reactivity, magnetic properties and also permittivity by varying the kinetic energy of the deposited particles.

The PLD process is started by placing the substrate and the target material in the vacuum chamber. Both targets, SrRuO_3 and BSBT were deposited using stoichiometric targets. A schematic of the PLD system used in this study can be seen in Figure 2.1.

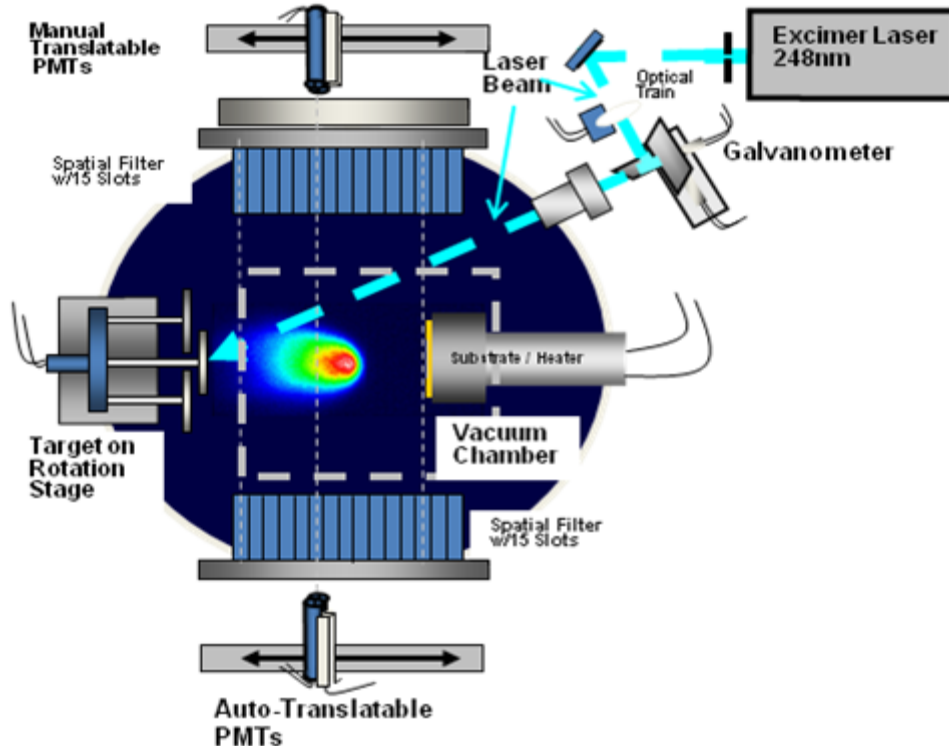


Figure 2.1. A diagram of the PLD chamber used for thin film growth.

Here the $(0.3)\text{BiScO}_3-(0.7)\text{BaTiO}_3$ target was prepared by mixing batching Bi_2O_3 and stoichiometric BaTiO_3 powders with 5 mol % excess Bi_2O_3 . The density of the target material is important to ensure a smoothness of the film deposited for a given laser fluence. A target that was too dense, such as a bulk single crystal, would not ablate properly without a laser fluence high enough to obtain a plume with a composition congruent with the target, leading to a thin film with improper stoichiometry [15]. It is also possible for the target to have a density too low leading to unfavorable ablation, because the target would ablate too easily causing a large distribution of particle sizes

to be ejected. The ideal target density (typically 98%) was one that allowed for uniform ablation of all target constituents in order to grow a thin film with proper stoichiometry.

In order to create partial pressure of oxygen, the chamber was first evacuated then backfilled with O_2 . Certain materials, such as the oxide used in this research, required a background gas to be present in the chamber during deposition. The oxide material was prone to losing oxygen if the chamber was under vacuum; a process called reduction. The background gas used for these materials was O_2 , allowing for the replacement of lost oxygen in order to obtain the correct stoichiometry of the thin film.

High-intensity short pulses (typically 17 ns) were focused on to the targets that were attached to a rotation stage to allow for uniform ablation. The energy absorbed by the target from the laser pulse was converted to electronic excitation resulting in thermal, chemical and mechanical energy leading to the release of a cone shaped plume of material containing atoms, ions, electrons, and particulates of the target material in a direction normal to the surface of the target. The plume displayed an angular distribution of target material with lighter particles spreading at larger oblique angles from the plume axis while the heavier particles traveled closer to the center. The angular distribution required adjustment of the target-substrate distance as well as the angle of the substrate with respect to the target depending on the elements within the target.

Our PLD system has a limitation of 7.1 cm target-substrate distance with little flexibility in the substrate angle. The chamber was equipped with two sets of photo-

multiplier tubes (PMTs) set behind narrow band-pass filters mounted to the exterior to monitor emission of excited elements within the plume. The PMTs were used to monitor the, time-of flight (TOF), time from initial target impact of the laser pulse to the time of maximum emission of a particular species as the components pass the PMT in order to maintain consistency between depositions. The adjustment of the laser voltage and chamber pressure affected the TOF. Higher oxygen pressures decreased the kinetic energy of the plume and higher laser voltage increased it.

For particles that reached the substrate, mobility was limited by their kinetic energy. Thus, the resulting structure was dependent on the temperature of the substrate which was typically heated to 650°C – 750°C creating a favorable energy condition to allow the film to grow in a crystalline structure. Energy from the heated substrate is absorbed by the particles allowing them to diffuse throughout the surface of the substrate where they were able to locate low energy sites creating a stable structure. When the appropriate substrate temperature was not provided, the resulting thin film was amorphous. This was due to the fact that crystallinity of thin films is determined by the bonding configurations of the atoms at a given temperature with the lowest free energy [16]. The deposition was continued until the desired film thickness of 330 nm was reached which was determined by a sensor which measured the material deposited per pulse and extrapolated for the total time of deposition. This yielded the desired final results in the form of stoichiometric thin films.

2.1.2 Growth Conditions

The growth conditions used in the PLD system were monitored and controlled using LabVIEW software. Parameters that were monitored during the depositions included: laser voltage, pulse energy, background gas pressure, laser repetition rate, total deposition time, substrate temperature, and TOF. Here the laser voltage and energy parameters were varied in order to maintain constant TOF. The background gas pressure was applied by evacuating the chamber to 10^{-7} Torr and back filling it with O_2 . A summarized list of the thin films that were grown along with the growth conditions is given in Table 2.1

Sample (#)	O ₂ Pressure (mTorr)	Laser Voltage (kV)	Rep Rate (Hz)	Substrate Temp. (°C)	Pulse Energy (mJ)	TOF (μs)
3491	100	16.6	10	700	442.6	5.01
3495	50	16.0	10	700	365.8	4.57
3501	50	16.0	10	750	332.6	4.77
3503	100	16.4	10	750	429.0	5.00
3505	100	17.1	10	650	466.9	4.99
3507	50	16.3	10	650	346.1	5.00

Table 2.1. Thin films grown with deposition parameters.

3 Material Characterization

The thin films in Table 2.1 were examined using X-Ray Diffraction (XRD) and AFM imaging. XRD measurements were used to gain insight to properties such as lattice parameters and spacing of the thin films, whereas the AFM imaging revealed the morphology of the thin films. Finally the grain sizes for each of the samples were calculated using XRD data and compared to the visually approximated values from AFM imaging.

3.1 X-Ray Diffraction

The technique of X-Ray Diffraction (XRD) is based on Bragg's law, which is explained in Figure 3.1. This method used the basic principles of diffraction and interference of electromagnetic waves.

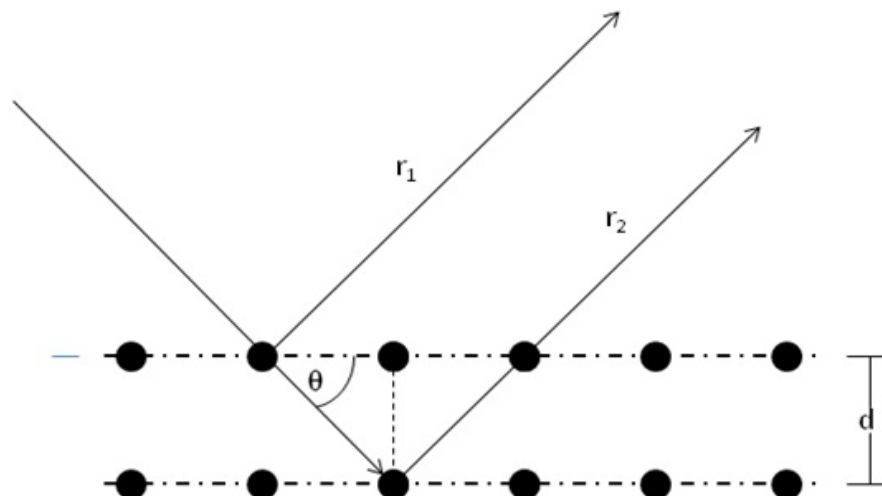


Figure 3.1. Diagram of Bragg's Law.

When light is passed through a material with periodic spacing between the planes in its crystal structure, interference occurs. However, one of the rays must travel $2d\sin\theta$ more than the other. The condition for constructive interference when X-rays are diffracted from a set of lattice plane is described by Equation 3.1, where λ is the wavelength of the incident light.

$$2d \sin \theta = n\lambda \quad n = 1,2,3, \dots \quad (3.1)$$

XRD measurements were performed using a Rigaku DMAX B diffractometer. The diffractometer consists of a X-ray source, a sample mount, and a detector. In the source, a beam of electrons is incident on a copper (Cu) target. This results in the target emitting $\text{CuK}_{\alpha 1}$ radiation with a wavelength of 0.154 nm. This is caused by the incident electrons dislodging an electron in the K shell of the Cu and an electron in the L shell dropping to fill the empty level. These emitted X-rays were then projected onto the

sample. Interaction with the lattice causes a portion of the X-Rays to diffract. The detector is attached to a goniometer. This gives the ability to rotate through a varying range of angles detecting the diffracted X-rays.

By plotting the intensity of detected X-rays vs. angle, peaks for every orientation allowing constructive interference can be analyzed. The lattice spacing of each sample can then be determined using Bragg's law with the known wavelength of the X-rays and the θ terms taken from each peak on the intensity plot. Orientations of the thin films are calculated by matching the lattice spacing values with a crystallographic database provided by the International Centre for Diffraction Data (ICDD).

3.2 Atomic Force Microscopy

Atomic Force Microscopy (AFM) is a branch of Scanning Probe Microscopy (SPM). This technique of microscopy uses a physical probe to create an image of a specimen instead of optical elements. The image is created by mechanically moving the probe across the sample surface line by line and measuring the probe surface interaction.

The very first development in the SPM technique was construction of the Scanning Tunneling Microscope (STM). The STM was developed by Gerd Binnig and Heinrich Rohrer in the early '80s at the IBM Research Laboratory in Ruschlikon, Switzerland, who won the Nobel Prize in 1986. However, this technique was restricted to electrically conducting surfaces because this method is based on measuring the

quantum tunneling current between the conducting tip and the sample when a potential difference is applied.

An extension of this technique, called the Atomic Force Microscopy (AFM), was developed by Gerd Binnig, Calvin Quate and Christopher Gerber. The AFM also allowed insulating materials to be analyzed. Here, very small sharp probing tip is scanned very closely above the sample surface. The distance between the sample surface and the probing tip is so small that the atomic range forces act between them. In order to measure these forces the probing tip is attached to a cantilever, where the deflection can be recorded. An enlarged photo of a cantilever probe arrangement is shown in Figure 3.2.



Figure 3.2. 228 μm long micro-fabricated silicon cantilever with integrated tip.

The deflection of the cantilever is detected by reflecting a laser beam off the top side of the cantilever. The deflection signal is then used in a feedback loop, as an error signal, to keep the cantilever deflection constant by expanding/contracting piezoelectric material. The system that varies the position is known as the Z controller. The local

height of the sample can be found by recording the change in piezoelectric material, creating a 3D map of the sample surface. This technique is referred to as the Static mode or the Contact mode.

Dynamic mode or Tapping mode is another technique of AFM. Here the cantilever is oscillated with fixed amplitude and a frequency close to the resonance frequency of the cantilever. The repulsive forces exerted by the sample on the tip increase the resonance frequency of the cantilever causing the vibration amplitude to decrease. This amplitude change is measured using the same detection system used to measure the deflection. Now the amplitude signal is used in a feedback loop similar to the Static mode.

3.2.1 Imaging

We have examined the morphology of each samples listed Table 2.1 by using a Nanosurf Easyscan 2 AFM manufactured by Nanosurf. The AFM was controlled using Nanosurf Easyscan 2 control software version 3.0. The Nanosurf Easyscan 2 controller attached to the AFM scan head is shown in Figure 3.3.



Figure 3.3. Nanosurf Easyscan 2 controller with the AFM scan head.

All the images were taken in Static force mode. Imaging in the Static force mode requires a set value for the working point of the cantilever which was set to 20 nN. Imaging in the Contact mode requires a free running feedback. This keeps the z-controller active and maintains the interaction between the sample surface and the cantilever. This was done using an Adaptive PI algorithm rather than the standard PID algorithm in order to reduce noise. Choosing the Adoptive PI against standard PID was a tradeoff between noise reduction and accuracy of fast topography changes. The standard PID algorithm uses the strength of the error signal (P-Gain), the strength of the integral of the error signal (I-Gain) and also the derivative of the error signal (D-gain) to calculate the strength of the z-controller reaction. A high I-gain reduces the error signal over time thus reducing a high frequency noise. On the other hand, the D-gain reduces the fast changes in the error signal but it also amplifies high frequency noise. Since the adoptive PI algorithm does not use a D-gain it eliminates high frequency noise but since fast changes in the error signal are not reduces the microscope is unable to capture

topography changes that happen faster the time between two measured points. The adoptive PI algorithm also varies the bandwidth of the topography measurement to match the number of measured points per second.

The imaging was done using an ANSCM-PT cantilever manufactured by AppNano. The cantilever was chosen to accommodate imaging requirements as well as electrostatic force measurement requirements, which are described in detail in Chapter 4. The complete specifications of the cantilever can be seen in Table 3.3. Using this configuration we scanned $5\text{ }\mu\text{m} \times 5\text{ }\mu\text{m}$ areas for each of the thin films. The results are displayed in the form of color maps and 3D topography representations in Chapter 5.

Handle Chip	
Length (mm) × Width (mm) × Height (μm)	3.4 × 1.6 × 300
Cantilever	
Material	Si
Shape	Rectangular
Reflex side coating	Pt/Ir
Reflex coating thickness (nm)	25 ± 5
Nominal spring constant (N/m)	3.0
Spring constant range (N/m)	1.2 – 6.4
Nominal Frequency (kHz)	62
Frequency range (kHz)	47 – 76
Length (μm)	225 ± 10
Width (μm)	60 ± 10
Thickness (μm)	3.0 ± 0.5
Tip Specifications	
Shape	Tetrahedral
Height (μm)	14 – 16
Radius of curvature (nm)	30
Coating	Pt/Ir
Coating thickness (nm)	25 ± 5

Table 3.1. ANSCM-PT Cantilever Specifications.

4 Measurement of Dielectric Constant Using AFM

4.1 Theoretical Background

Let us consider a thin film deposited by using PLD on a substrate along with an electrode, where the electrode is partially exposed and grounded. A conductive cantilever with a nano-sized tip is positioned over the sample as shown in Figure 4.1.

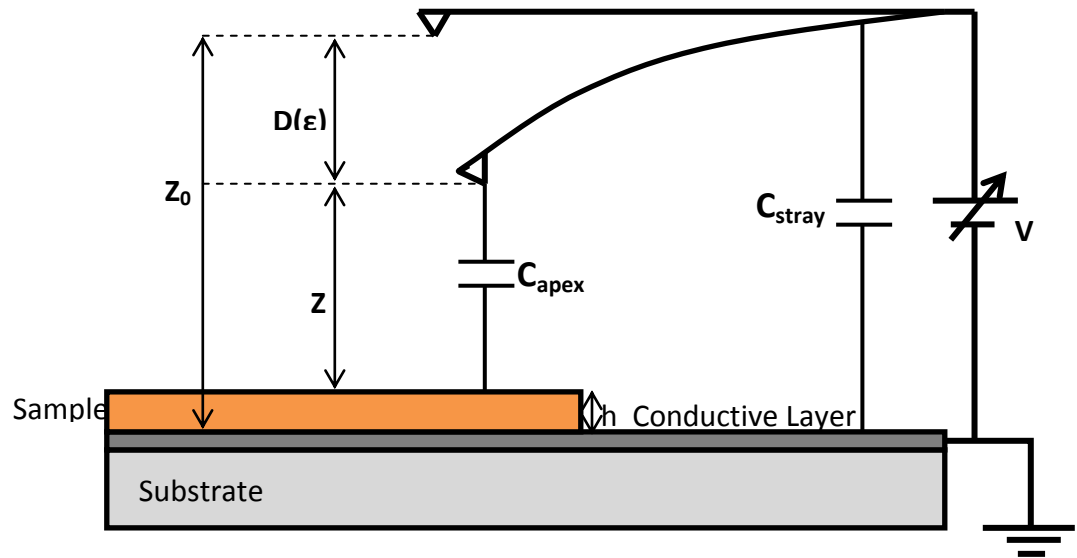


Figure 4.1. Dielectric measurement set-up of thin film sample deposited on a substrate with a conductive layer. A DC voltage bias is applied between the substrate and the cantilever. The resulting deflection D depends on the local dielectric constant of the sample.

Cantilever is positioned at a distance z_0 above the sample surface. A DC bias voltage is applied between the cantilever and the electrode creating an excess positive charge on the AFM probe causing the cantilever to deflect towards the more negatively charged sample surface by a distance D bringing the cantilever tip to a new equilibrium position z .

The equilibrium tip-sample distance at a given DC applied voltage corresponds to the minimum energy of the system consisting of the AFM probe and the sample. This system energy contains contributions from various forces acting on the AFM probe. Thus, the total energy of the system, E_T , can be expressed in the form of Equation 4.1.

$$E_T = E_K + E_{vdW} - E_C \quad (4.1)$$

Here, the recovering elastic energy, E_K , is represented as the elastic energy of a spring with a spring constant k corresponding to the spring constant of the cantilever (Equation 4.2).

$$E_K = \frac{1}{2}k(z_0 - z)^2 \quad (4.2)$$

The electrostatic probe-sample energy, E_C , is modeled as the energy of the capacitor between the probe and the substrate (Equation 4.3).

$$E_C = \frac{1}{2}C_T V^2 \quad (4.3)$$

where V represents the sample-probe DC bias voltage and C_T denotes total capacitance of the system.

The total capacitance of the system can be broken down into 3 components corresponding to each major segment of the AFM probe. The cantilever part C_l , cone C_c , and C_{apex} tip end (apex). We consider capacitance contributions from the micrometric parts of the AFM probe C_l and C_c as the stray capacitance C_{stray} . Therefore, the total capacitance of the system is represented by Equation 4.4

$$C_T = C_l + C_c + C_{apex} \quad (4.4)$$

Explicit expressions for each contribution to the capacitance (Equation 4.4) in terms of geometric properties of the AFM probe are derived in [17, 18]. The capacitance associated cantilever is represented by Equation 4.5 [17].

$$C_l = \frac{\epsilon_0 W \tan^2(\beta_{lever})}{\beta_{lever}^2 \tan(\beta_{lever}/2)} \ln \left[1 + \frac{2L \tan(\beta_{lever}/2)}{z + H} \right] \quad (4.5)$$

where W and L are the width and length of the cantilever, respectively, β_{lever} is the tilt angle of the lever and H is the height of the cone, whereas the new equilibrium position is denoted by z . Next, the capacitance contribution from the cone of the AFM probe is given by Equation 4.6 [17].

$$C_c = \frac{-8\pi\epsilon_0}{(\pi - \beta_{lever})^2} [f_1(\ln(f_1) - 1) - f_2(\ln(f_2) - 1) - \sin(2\theta)(H \ln(2f_1) - \delta \ln(2f_2))] \quad (4.6)$$

where θ is the half-cone aperture angle and R is the apex radius. Furthermore, $f_1 = z + H - \delta/2$, $f_2 = z + \delta/2$, and $\delta = R/[\tan^2(2\theta)]$. Finally, the capacitance part from the apex of the probe for a dielectric sample with relative dielectric constant ϵ_r and height h is described by Equation 4.7 [6].

$$C_{apex} = 2\pi\epsilon_0 R \ln \left[1 + \frac{R(1 - \sin\theta)}{z + \frac{h}{\epsilon_r}} \right] \quad (4.7)$$

Going back to Equation 4.1, the remaining energy contribution term coming from Van der Waals force [19] can be expressed as follows (Equation 4.8).

$$E_{vdW} = \frac{AR}{6r_0^2} \left[\frac{1}{28} \left(\frac{r_0^8}{z^7} \right) - \left(\frac{r_0^2}{z} \right) \right] \quad (4.8)$$

where A is the Hamaker constant, R is the radius of the tip apex and r_0 is the interatomic spacing (around 0.4 nm).

In order to derive a simplified expression we utilize the following approximations [20].

- I. The location of the electrostatic minimum is essentially determined by the electrostatic and elastic forces. This approximation holds as long as the location of the minimum is far enough from the substrate. At this location, the vdW forces are negligible (more than 6 nm).
- II. The capacitance contributions from the cantilever and the tip sum up to a contribution that varies linearly with the tip-sample distance. This approximation holds as long as the tip-substrate distance is less than a few hundred nanometers.

Taking these approximations into account (I and II) Equation 4.1 reduces to Equation 4.9

$$E_T = \frac{1}{2}k(z_0 - z)^2 - \frac{1}{2}C_T V^2 \quad (4.9)$$

Using Equation 4.9, we can easily calculate the minimum energy with respect to z

$$\frac{\partial E_T}{\partial z} = -k(z_0 - z) - \frac{1}{2} \frac{\partial C_T}{\partial z} V^2 = 0 \quad (4.10)$$

After rearrangement, we have

$$(z_0 - z) = -\frac{1}{2k} \frac{\partial C_T}{\partial z} V^2 \quad (4.11)$$

From approximation II, we can express a derivative of the total capacitance as follows

$$\frac{\partial C_T}{\partial z} \approx -F - f(z) \quad (4.12)$$

where

$$-F \approx \frac{\partial(C_l + C_c)}{\partial z} \quad (4.13)$$

and

$$\frac{\partial C_{apex}}{\partial z} = -f(z) = -\frac{2\pi\epsilon_0 R \tilde{R}}{\left(z + \tilde{R} + \frac{h}{\epsilon_r}\right)\left(z + \frac{h}{\epsilon_r}\right)} \quad (4.14)$$

with

$$\tilde{R} = R(1 - \sin \theta) \quad (4.15)$$

Substituting Equations 4.12-4.14 into Equation 4.11, we can end up with the following expression for the total deflection of the cantilever

$$D = z_0 - z = \frac{(V - V_{sp}(\epsilon_r))^2 \pi \epsilon_0 R \tilde{R}}{k} \left[\left(z + \tilde{R} + \frac{h}{\epsilon_r} \right) \left(z + \frac{h}{\epsilon_r} \right) \right]^{-1} + D_0(\epsilon_r) \quad (4.16)$$

Here, we have used $V - V_{sp}(\epsilon_r)$ as the effective bias voltage between the sample surface and the AFM probe where $V_{sp}(\epsilon_r)$ denotes the surface potential of the dielectric sample. In-depth derivation of the surface potential is given in the next section. In addition, the deflection caused by the capacitance contributions of the cantilever and the cone is represented by the constant D_0 . If we consider a metallic sample, $h/\epsilon_r \rightarrow 0$, reducing Equation 4.16 into Equation 4.17 [21].

$$D = \frac{(V - V_{sp})^2 \pi \epsilon_0 R \tilde{R}}{k} [(z + \tilde{R})z]^{-1} + D_0 \quad (4.17)$$

By re arranging Equation (4.16) the local dielectric constant ϵ_r can be expressed as a function of the cantilever deflection.

$$\epsilon_r(D) = 2h \left\{ -2z - \tilde{R} + \left([2z + \tilde{R}]^2 - 4z(z + \tilde{R}) + 4 \frac{(V - V_{sp}(\epsilon_r))^2 \pi \epsilon_0 R \tilde{R}}{k(D - D_0(\epsilon_r))} \right)^{\frac{1}{2}} \right\}^{-1} \quad (4.18)$$

Calculation of the remaining parameters (k , $V_{sp}(\epsilon_r)$, R , θ and $D_0(\epsilon_r)$) in equation 4.18 is discussed in the following section.

4.2 Parameter Calibration

4.2.1 Spring Constant

Spring constant k can be obtained by analyzing the thermal oscillation of the cantilever [22]. Treating the cantilever as a harmonic oscillator fluctuating in response to thermal noise yields the following Hamiltonian

$$H = \frac{p^2}{2m} + \frac{1}{2}m\omega_0^2 q^2 \quad (4.19)$$

where q is the displacement of the oscillator, p is the momentum, m is the oscillating mass and ω_0 is the resonant angular frequency of the system. By utilizing equipartition theorem we can say that

$$\langle \frac{1}{2}m\omega_0^2 q^2 \rangle = \frac{1}{2}k_B T \quad (4.20)$$

Here k_B denotes the Boltzmann constant and T represents the temperature. Since

$$\omega_0^2 = \frac{k}{m} \text{ we can simplify Equation 4.20 to obtain}$$

$$k = \frac{k_B T}{\langle q^2 \rangle} \quad (4.21)$$

where $\langle q^2 \rangle$ stands for the mean square displacement of the cantilever. Therefore the spring constant of the cantilever can be estimated by measuring the deflection of a freely moving cantilever at a sampling rate higher than the resonant frequency.

4.2.2 Surface Voltage

The surface voltage $V_{sp}(\epsilon_r)$ can be derived by measuring the electrostatic force between the tip and the sample when a varying bias voltage is applied. The electrostatic force between the tip and the sample can be written as a surface integral over the electric field on the sample surface.

$$F(z) = \int_S dS \frac{\epsilon_0}{2} [E(x, y, z)]^2 \quad (4.22)$$

where $E(x, y, z)$ is the electric field on the surface for a certain tip-sample distance z . In a typical SFM setup the electric field lines can be approximated by segments of circles connecting the tip and the sample with the electric potential decreasing linearly along these segments. Therefore Equation 4.22 can be written as

$$F(z) \cong \frac{\epsilon_0 V_0^2}{2} \int_S dS \frac{1}{[a(x, y, z)]^2} \quad (4.23)$$

where V_0 is the effective voltage between the tip and the sample and $a(x, y, z)$ is the arc length of the circular segment coming from the probe and ending on a point (x, y, z) of the surface. The effective voltage is $V_0 = V - V_{sp}(\epsilon_r)$, with V as the potential of the tip and $V_{sp}(\epsilon_r)$ as the surface potential of the sample

$$F(z) = \frac{C'(z)(V - V_{sp}(\epsilon_r))^2}{2} \quad (4.24)$$

Where $C'(z)$ is the derivative of the tip sample capacitance [23]. From Equation 4.24 we can say that the electrostatic force is a quadratic function of tip voltage, with its minimum shifted by an amount $V_{sp}(\epsilon_r)$ with respect to the origin.

4.2.3 Cone Angle

The cone angle θ of the AFM probe is related to the geometric shape of the cantilever tip. The cantilever used in this experiment has a regular tetrahedral tip shape. The cone angle in this situation is equal to the solid angle formed by the three faces of the tetrahedron at the apex of the tip.

The solid angle of a tetrahedron can be found using the following formula:

$$\sum_{i=1}^4 \Delta_i = \left[2 \left(\sum_{i=1}^6 \delta_i \right) - 4\pi \right] R^2 \quad (4.25)$$

where Δ_i is the area of the spherical triangle formed by the i 'th face of a tetrahedron in a sphere of radius R and δ_i is the angle subtended by edge i . For a regular tetrahedron, we can replace δ_i with $\cos^{-1}(1/3)$ and obtain the solid angle θ as follows

$$\theta = \frac{\Delta_i}{R^2} = 3 \cos^{-1}\left(\frac{1}{3}\right) - \pi \quad (4.26)$$

4.2.4 Tip Radius

The tip radius R can be found using Equation 4.17. A deflection versus distance curve taken over the SrRuO_3 metallic buffer layer (see Figure 4.1) can be fitted to Equation 4.17 in order to extract R . Note that the z range for the fit function has to be selected to comply with approximation I and II in section 4.1. Also previously derived values for the cone angle, surface potential and the spring constant are needed for calculation of the tip radius. Here D_0 can be treated as a free parameter.

4.2.5 Stray Deflection

The stray deflection value $D_0(\epsilon_r)$ of the AFM probe can be obtained by monitoring the deflection at higher z distances. When the distance between the tip and the sample is increased the deflection contribution from the apex of the cantilever becomes negligible and the total deflection approaches a value equal to $D_0(\epsilon_r)$ (see Equation 4.16). Thus, taking the average of a deflection distance curve around 180 nm away from the sample surface will provide an approximate value of $D_0(\epsilon_r)$.

4.3 Procedure

4.3.1 Sample Preparation

The samples were prepared for measurement by etching away a part of the top-layer of BSBT thin film to expose the conductive SrRuO₃ layer deposited on the LSAT single crystal substrate. This was accomplished by sputter etching the sample in the MRC Sputtersphere. A power level of 600 W was maintained for 15 minutes during this process. The conductivity was monitored during the process and the sudden change in conductivity at a 330 nm confirms the exposure of the SrRuO₃ layer. A plot of a cross-sectional profile after etching is presented in Figure 4.2. Exposed conductive layer is then grounded using a drop of silver paint as it can be seen in Figure 4.3.

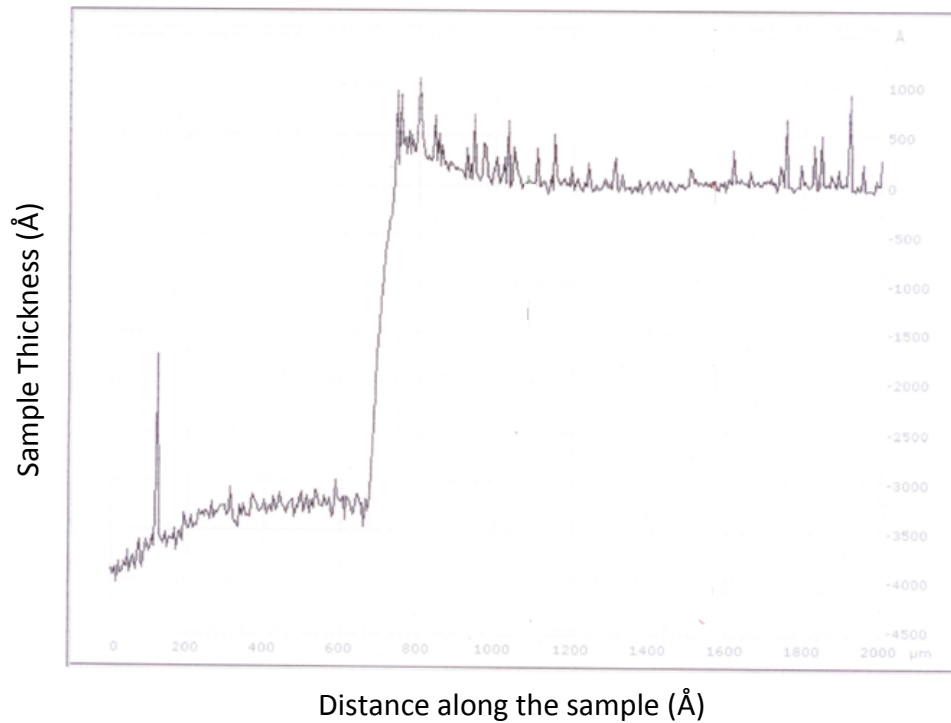


Figure 4.2. Cross section of the sample after etching showing an etch depth of 330 nm.

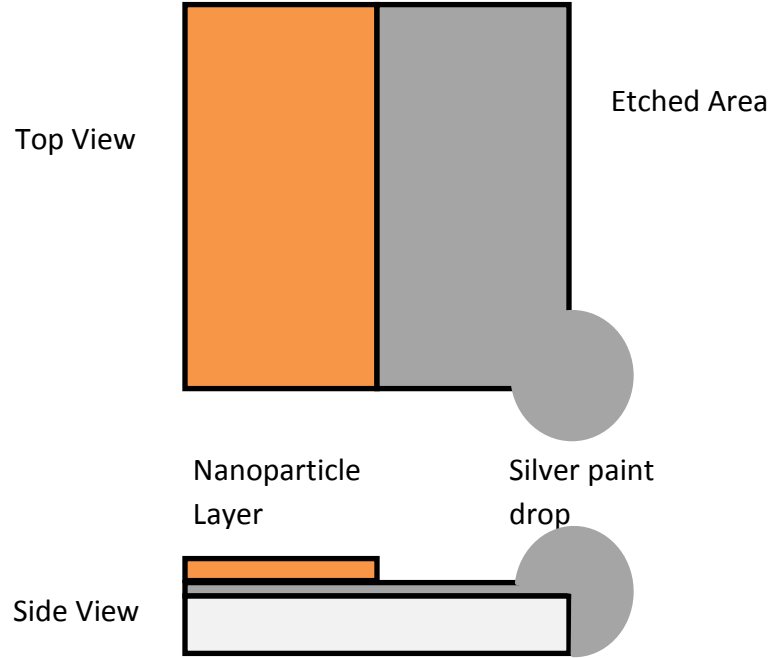


Figure 4.3. Sample prepared for measurement with grounded created by using silver paint drop.

4.3.2 Measurement Protocol

As the first step, the cantilever tip was positioned above the exposed conductive region of the sample. The sample was approached using the step motor of the AFM until a 20 nN force was experienced by the cantilever. After this the feedback signal was disabled. Next, a deflection vs. distance measurement was made by varying the z position of the cantilever. This data was recorded as a spectroscopy measurement with a time modulation of 0.1 seconds. This spectroscopy measurement was used to find the tip radius R as described in section 4.2.2.

After the measurements on the conductive layer were completed, the BSBT thin film layer was positioned under the cantilever tip. After activating the feedback loop the

sample was approached in a similar fashion and a topography image was created in Static mode to obtain the morphology of sample. Next, a deflection versus distance spectroscopy measurement was made, moving the cantilever away from the sample surface. This technique is used to set z_0 by specifying the desired value of 100 nm as the final value for the spectroscopy measurement. Once the equilibrium position z_0 was established, a voltage bias of 10 V was applied between the cantilever and the conductive layer of the sample. Then we recorded the deflection of the cantilever over 0.1 seconds maintaining the scan height and the applied voltage constant. The average value of this measurement was taken as the total deflection. Next, a second deflection versus distance curve was obtained by varying z up to a distance of 200 nm above the sample surface. From this measurement, we calculated the stray deflection $D_0(\epsilon_r)$ by taking the average of the deflection after it approached constant value. By substituting each of these quantities in Equation 4.18, we obtain a dielectric constant value for the given sample.

5 Results

5.1 Atomic Force Microscopy

AFM images were acquired for an area of $5\text{ }\mu\text{m} \times 5\text{ }\mu\text{m}$ for each sample. The morphology and approximate grain sizes were visually analyzed using the color maps and 3D AFM images for each BSBT sample. Additionally, line profiles were created to approximate roughness for each sample. A color map for sample # 3505 is displayed in Figure 5.1.

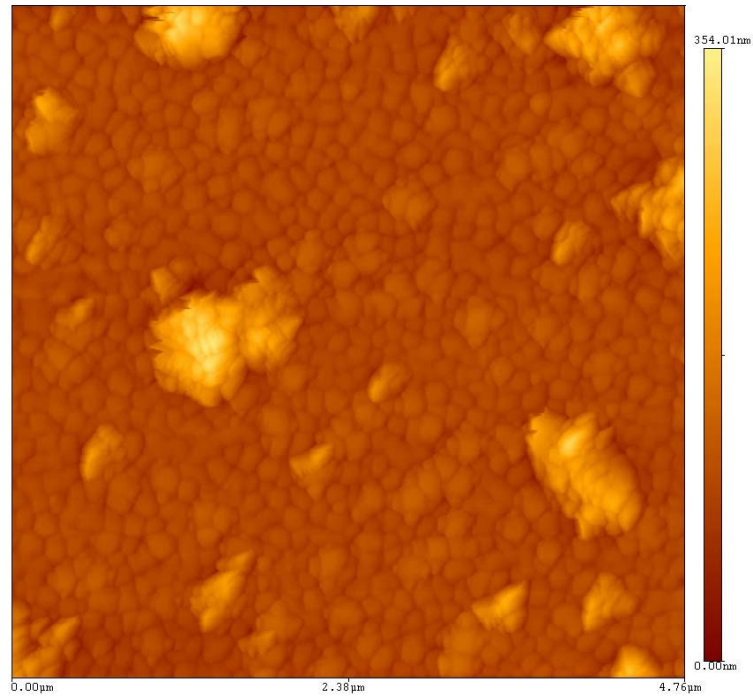
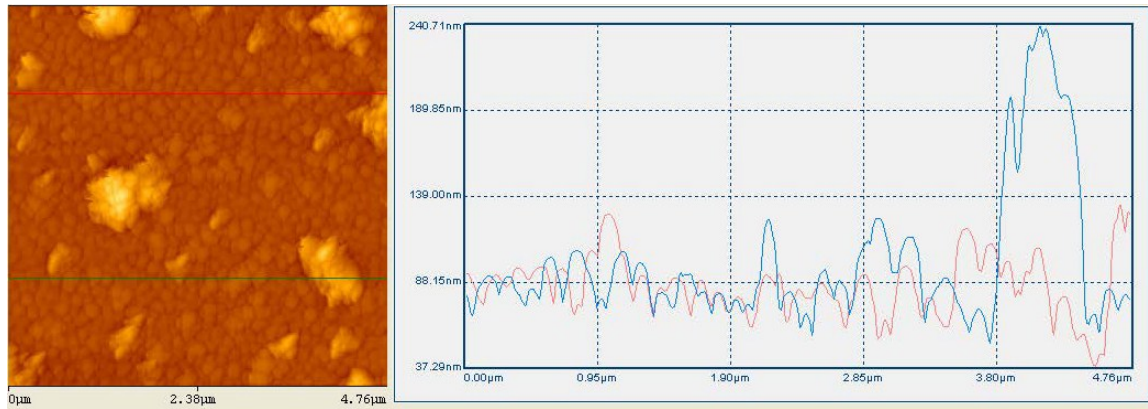


Figure 5.1. $5\text{ }\mu\text{m} \times 5\text{ }\mu\text{m}$ color map of BSBT sample #3505.



(a) (b)
Figure 5.2. Line profiles (b) for BSBT sample # 3505 (a).

Figure 5.2 shows the line profiles created for the color map in Figure 5.1. The red line was chosen to avoid abnormalities such as outgrowths and the green line included an outgrowth. The average roughness calculated for the red line was 13.5 nm while for the blue line a displayed roughness was 27.8 nm. The average roughness of the same area for each sample was calculated by taking multiple line profiles across the area. Color maps for each sample along with the average roughness peak to valley differences are presented in Table 5.1.

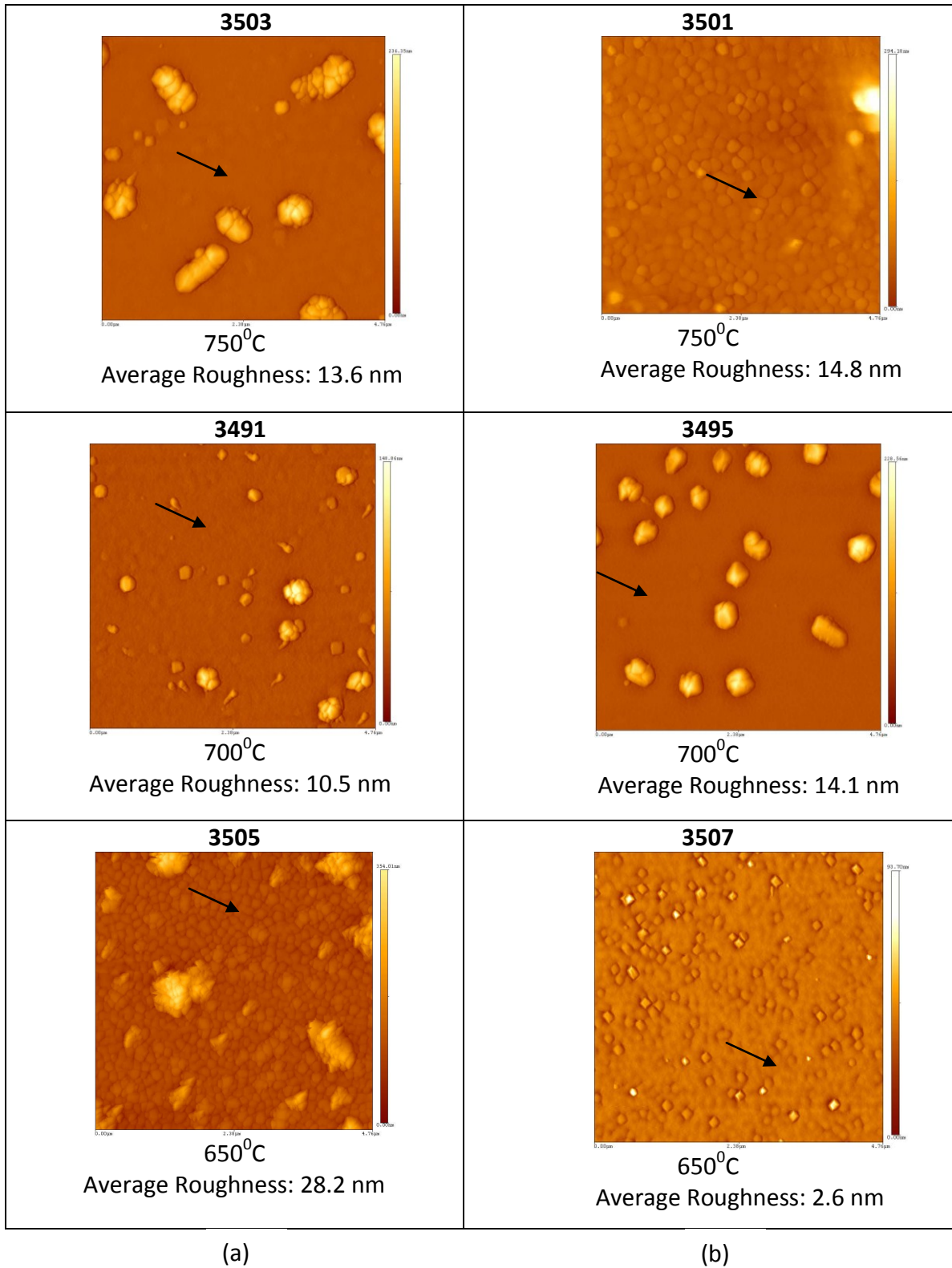


Table 5.1. Color maps of BSBT thin films deposited at different temperatures and two partial oxygen pressures (100 mTorr, a) and (50 mTorr, b), respectively together with average roughness. The locations of ϵ_r measurements are represented by arrows.

5.2 X-Ray Diffraction

The intensity versus angle 2θ was plotted to analyze XRD data for sample # 3505. We observed three <200> peaks in intensity, which were related to the BSBT thin film, the SRO conductive buffer layer and the LSAT substrate, respectively. The BSBT thin film was fitted to a Gaussian curve. As an example, intensity versus angle plot for sample # 3505 (650 °C, 100 mTorr) can be seen in Figure 5.2. The peak located at $(2\theta) = 35.51^\circ$ is fitted to a Gaussian curve with a FWHM value of 1.02° . The θ , FWHM and the grain size acquired from Scherrer formula for each sample is summarized in Table 5.2.

$$d = K \lambda / (\beta \cos \theta) \quad (5.1)$$

where d represents the grain size, λ is the radiation wavelength (0.154 nm), β is the width at half the maximum intensity, θ is the Bragg angle and the constant K (usually equal to 0.9) stands for the shape factor.

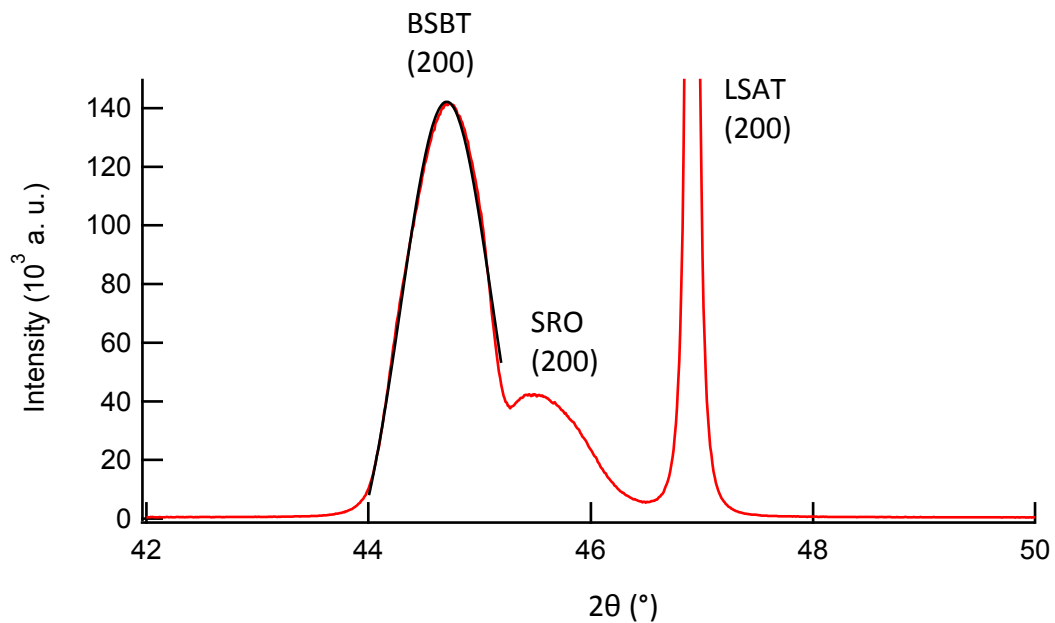


Figure 5.3. Intensity versus 2θ angle for BSBT sample (# 3505) with Gaussian fit.

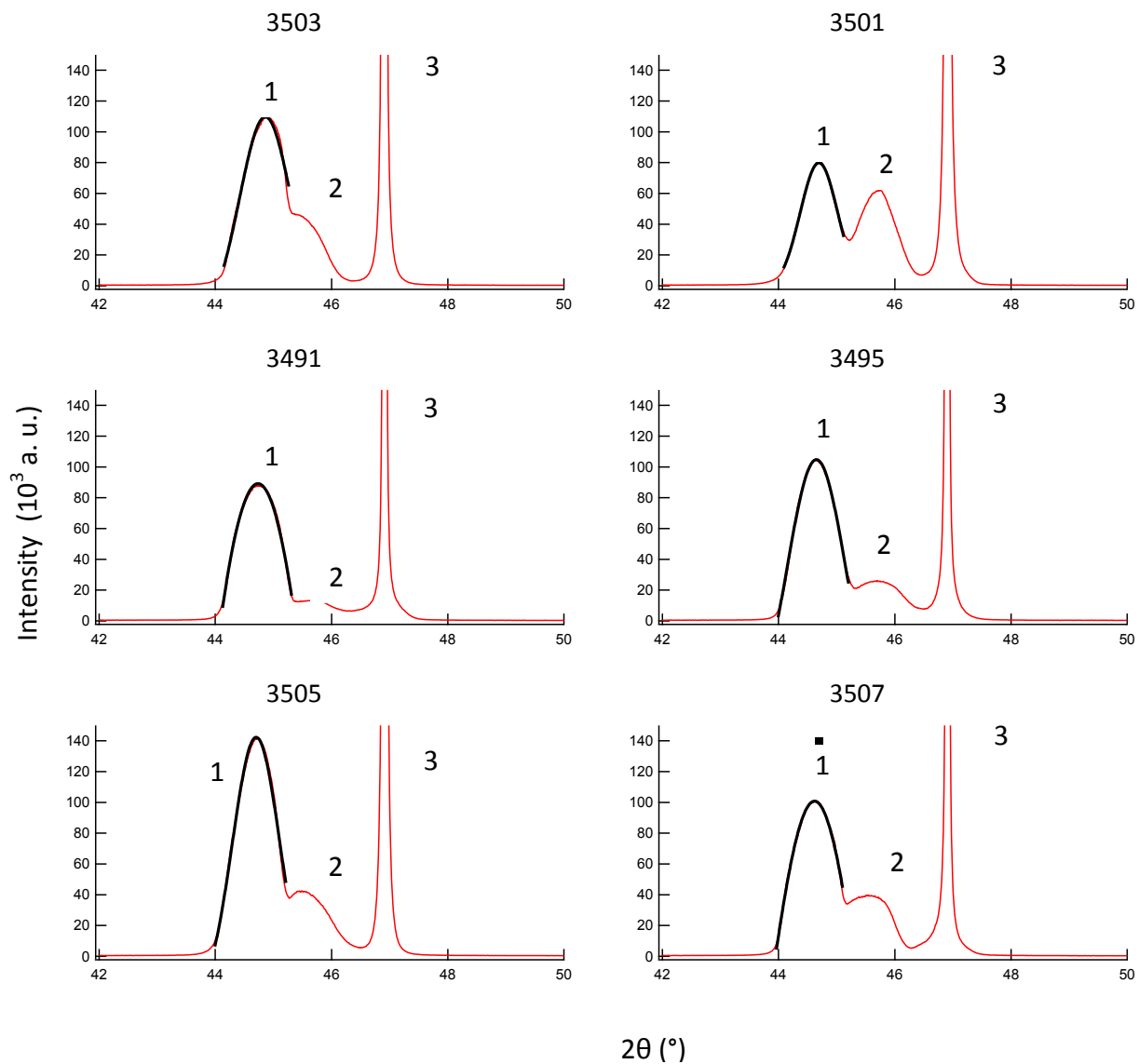


Table 5.2. Intensity versus 2θ for each sample. Here peaks 1, 2 and 3 represents BSBT(200), SRO(200) and LSAT(200), respectively. Peak # 1 of each sample is fitted with a Gaussian curve.

Sample (#)	θ (radian)	FWHM (radian)	Grain size (nm)
3491	0.3905	0.0159	9.44
3495	0.3895	0.0147	10.23
3501	0.3900	0.0129	11.60
3503	0.3920	0.0150	9.99
3505	0.3904	0.0145	10.35
3507	0.3894	0.0161	9.33

Table 5.3. Grain sizes calculated from BSBT (200) X-ray diffraction peaks.

5.3 Dielectric Constants

Deflections were measured, with a varying z , over the etched area of the samples.

The data were fitted to Equation 4.17 using Igor Pro version 6.2. The fitting was restricted for a selected range of z values where Equation 4.17 is valid (30 nm – 100 nm from the sample surface).

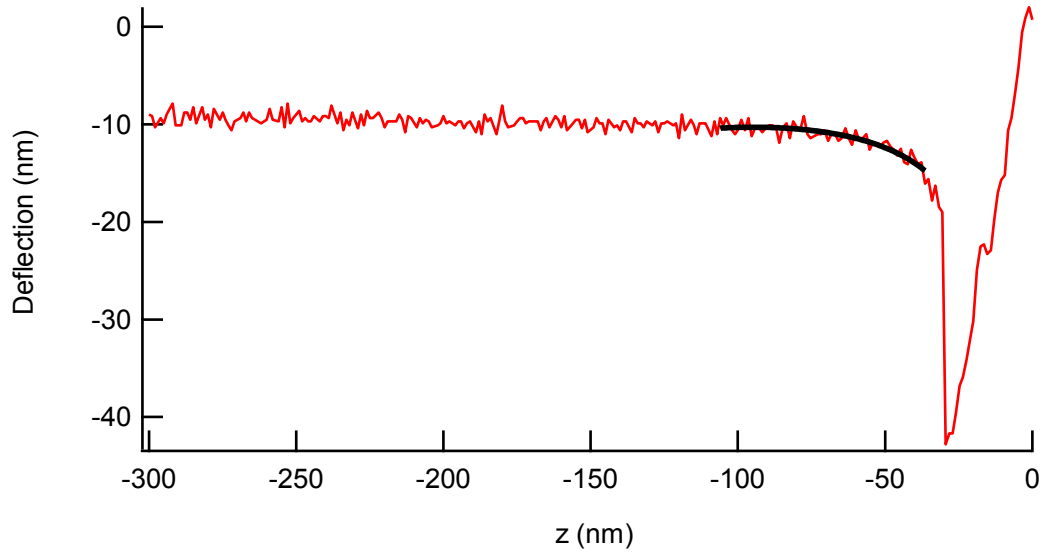


Figure 5.4. Deflection versus z distance with Equation 4.17 fitted from $z = 100$ nm to $z = 30$ nm above the metallic buffer layer.

The deflection is plotted versus z in Figure 5.4. By fitting data to Equation 4.17 we obtained 358.1 nm as the tip radius.

The deflection under an applied DC bias voltage ranging from -5 V to 5 V between the cantilever and the bottom electrode was obtained over the dielectric material. The tip position was maintained at 100 nm over the sample surface. Figure 5.5 shows a plot of the deflection versus voltage taken for sample # 3501. The data was fitted to a parabolic function. The minimum deflection according to the fit function occurs at 0.85 V which is equal to the surface voltage at that point. The surface voltage values for the remaining points and the samples are shown in Table 5.3.

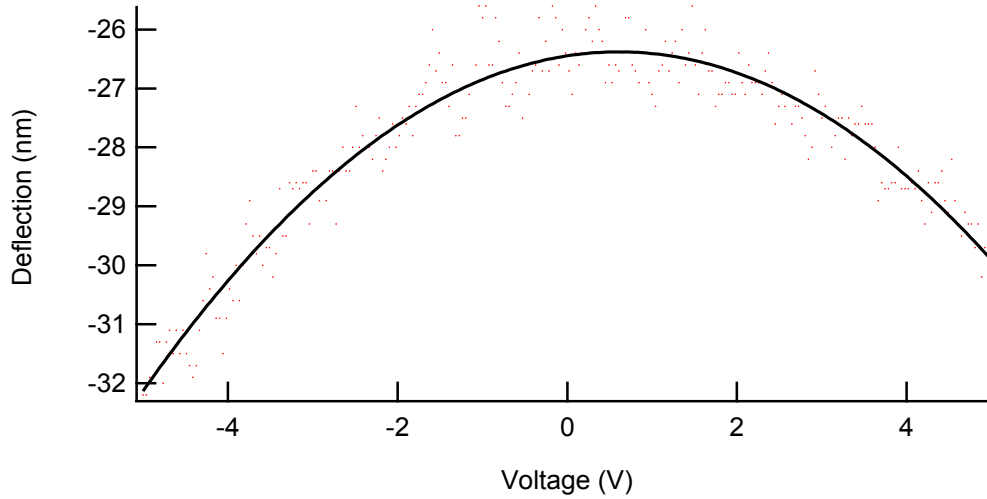


Figure 5.5. Deflection versus voltage for sample # 3501 measured 100 nm above the sample at coordinates (2.05,-1.05).

The static deflection under a constant DC bias of 10 V was acquired by averaging the deflection over a period of 0.1 seconds. Measurement taken at coordinates (2.05,-1.05) on sample # 3505 displayed an average deflection of 10.4 nm. Using a tip radius of 358.1 nm, a cone angle of 31.6° and a spring constant of 3 N/m, the dielectric constant for the specific location (2.05,-1.05) on sample # 3505 was calculated to be 22.2. Here reference z plane was set at the surface of the sample resulting in equilibrium position z of 89.58 nm. In addition, the boundary between the BSBT layer and the SRO buffer layer is located at 330 nm below the reference $z=0$ plane.

Next, as seen in Figure 5.6, we measured the deflection with an increasing distance above the sample and approximated the stray deflection ($D_0(\epsilon_r)$) by taking the average deflection after it approached a constant value.

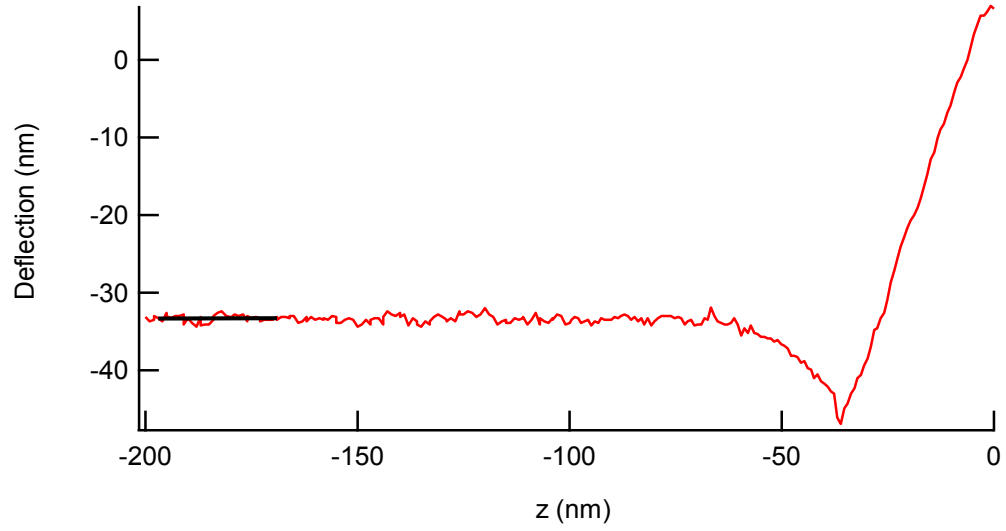


Figure 5.6. Deflection versus z distance with the average taken around 180 nm above the sample # 3501.

The total deflection (D), stray deflection ($D_0(\epsilon_r)$), surface voltage ($V_{sp}(\epsilon_r)$) and the equilibrium position (z) for each sample is summarized in Table 5.4 along with the calculated relative dielectric constant (ϵ_r).

Sample (#)	D (nm)	$D_0(\epsilon_r)$ (nm)	$V_{sp}(\epsilon_r)$ (v)	z (nm)	ϵ_r
3491	30.1	27.6	0.68	69.9	40.6
3495	20.9	-----	0.48	79.1	-----
3501	36.1	33.4	0.85	63.9	42.0
3503	45.2	42.1	1.33	54.8	69.1
3505	10.4	8.6	0.53	89.6	22.6
3507	19.1	-----	0.33	80.9	-----

5.4. Deflection, stray deflection, surface voltage, equilibrium position and the dielectric constant, respectively calculated for each BSBT sample.

6 Discussion and Conclusions

In this Chapter, we will discuss structural and electrostatic properties of $0.3\text{BiScO}_3 - 0.7\text{BaTiO}_3$ samples prepared by using PLD process under the following conditions: (100) LSAT single crystal substrate temperatures were at 650 °C, 700 °C and 750 °C and deposition took place under 50 mTorr and 100 mTorr partial oxygen pressure (see Table 2.1). In addition, a metallic buffer layer was deposited between the BSBT thin films and the LSAT at the elevated temperature of 750 °C and 300 mTorr of partial oxygen pressure to provide the bottom electrode required for electrostatic measurements. These measurements were done using an Atomic Force Microscope which enables us to record the interaction between the probe and the BSBT sample in terms of cantilever deflection. Theoretical model discussed in Chapter 4 allows to connect sample depended cantilever deflection with the dielectric constant of the material under investigation (see Equation 4.18).

XRD diffraction patterns (see Table 5.2) suggest that the best stoichiometric sample was fabricated at 750 °C substrate temperature and 50 mTorr partial pressure of oxygen with distinct (200) peaks of LSAT, SRO and BSBT (# 3501). In addition, this sample has the highest average roughness and the largest grain size $d = 11.6 \text{ nm}$ (see Table 5.1 b) based on AFM topography (Figure 5.2) and XRD analysis using Scherrer formula

(Equation 5.1), respectively. However, we were unable to obtain roughness values for samples # 3505 and # 3501 because of abnormalities such as outgrowths.

Dielectric constants for the BSBT samples were calculated using the measurements summarized in Table 5.4. In these calculations, I have used the manufacturer provided value for the spring constant instead of the value obtained from thermal oscillations as discussed in section 4.2.1. Since the thermal oscillations are in the range of few Angstroms, a very high uncertainty was associated with the calculation due to noise and the uncertainty in deflection measurements associated with the AFM. Also the stray deflection values for samples # 3507 and # 3495 were unobtainable since the deflection did not approach a constant value within the measured z range. According to the results presented in Chapter 5, the total uncertainty for the dielectric constant, $\sigma(\epsilon_r)$, was calculated to be 1.7. Although, there are several parameters in Equation 4.18, the main source of uncertainty comes from the deflection detection system of the AFM. We also observed a difference between the manufacture provided tip radius and the tip radius obtained from the technique discussed in Chapter 4. In this situation, experimental value was used in the calculations because of the deformation and wear that occurs in the AFM tip especially after contact mode imaging [24].

In conclusion, we have summarized the properties for the six BSBT samples that were examined in this study (see Table 6.1). Here, we have grouped the samples by the partial oxygen pressure used in the PLD process and arranged them according the increasing substrate temperature.

Sample (#)	Substrate Temp. (°C)	O ₂ Pressure (mTorr)	Grain Size (nm)	Roughness (nm)	ϵ_r
3505	650	100	10.35	28.2	22.6
3491	700	100	9.4	10.5	40.6
3503	750	100	10.0	13.6	69.1
3507	650	50	9.3	2.6	-----
3495	700	50	10.2	14.1	-----
3501	750	50	11.6	14.8	42.0

Table 6.1. Summary of fabrication conditions, grains sizes, roughness values and dielectric constants for the six BSBT samples.

Comparing the grain sizes for each pressure shows that the increasing substrate temperature causes the grain size to increase. The roughness values obtained from AFM line profiles also support this pattern. For each of the three temperatures, using a lower O₂ pressure has resulted in a smaller grain size and lower roughness. The samples fabricated under 100 mTorr of pressure suggest that using a higher substrate temperature of 750°C yields a larger dielectric constant $\epsilon_r = 69.1$

Taking a series of measurements over the sample surface would allow us to map the dielectric constant on the surface of the sample and also provide a more general average value over the entire sample. However, our goal in this study was to identify the optimal growth conditions, thus we were testing virgin samples that were not exposed to any external electric field. Since our measurement method required a DC electric field

to be applied to our samples, we were already polarized them after analyzing the very first point on the sample. This point was carefully chosen to represent the area of the sample avoiding outgrowths as seen in Table 5.1.

In future work, a better precision for deflection measurements can be achieved by using, for example, lock-in amplifier. Our assumption, in the current study, was to make AFM measurements without using any additional electronic devices.

7 Bibliography

- [1] Stern J E, Terris B D, Mamin H J and Rugar D, "Deposition and imaging of localized charge on insulator surfaces using a force microscope", *Applied Physics Letters*, vol. 29, p. 363, 1988.
- [2] O'Hayre R, Lee M and Prinz F B, "Ionic and electronic impedance imaging using atomic force microscope", *Journal of Applied Physics*, vol. 95, p. 8382, 2004.
- [3] Hu J, Xiao X D and Salmeron M, "Scanning polarization force microscopy - a technique for imaging liquids and weakly absorbed layers", *Applied Physics Letters*, vol. 67, p. 476, 1995.
- [4] Lynch B P, Hilton A M and Simpson G J, "Nanoscale dielectrophoretic spectroscopy of individual immobilized mammalian blood cells", *Biophysics*, vol. 95, p. 2678, 2006.
- [5] Kalinin S V, Karapetian E and Kachanov M, "Nanoelectromechanics of piezoresponse force microscopy", *Physics Review B*, vol. 70, p. 184101, 2004.
- [6] Gramse G, Casuso I, Toset J, Fumagalli L and Gomila G, "Quantitative dielectric constant measurement of thin films by DC electrostatic force microscopy",

Nanotechnology, vol. 20, p. 395702, 2009.

- [7] Gramse G, Toset J and Fumagalli L, "Nanoscale capacitance microscopy of thin dielectric films", *Journal of Applied Physics*, vol. 104, p. 024315, 2008.
- [8] Fumagalli L, Ferrari G, Sampietro M, Casuso I, Martinez E, Samitier J and Gomila G, "Nanoscale capacitance imaging with attofarad resolution using ac current sensing atomic force microscope", *Nanotechnology*, vol. 17, pp. 4581, 2006.
- [9] Ferrari G and Sampietro M, "Wide bandwidth transimpedance amplifier for extremely high sensitivity continuous measurements", *Review of Scientific Instruments*, vol. 104, p. 094703, 2007.
- [10] Fumagalli L, Ferrari G, Sampietro M and Gomila G, "Dielectric-constant measurement of thin insulating films at low frequency by nanoscale capacitance microscopy," *Applied Physics Letters*, vol. 91, p. 243110, 2007.
- [11] Fumagalli L, Ferrari G, Sampietro M and Gomila G, "Quantitative nanoscale dielectric microscopy of single layer supported bio membranes", *Nano Letters*, vol. 9, p. 1604, 2009.
- [12] Tinberg D S and Trolier-McKinstry S, "Structural and electrical characterization of $x\text{BiScO}_3-(1-x)\text{BaTiO}_3$ thin films", *Applied Journal Of Physics*, vol. 101, p. 411, 2007.
- [13] Chrisey D B and Hubler G K, *Pulsed Laser Deposition of Thin Films*, New York: Wiley,

2003.

- [14] Hayward S A, Redfern S A T and Salje E K H, "Order parameter saturation in LaAlO_3 ", *Journal of Physics: Condensed Matter*, vol. 14, p. 10131, 2002.
- [15] Yang R, Shen S Y and Wang C B, "Composition controlling of KNbO_3 ", *Materials Letters*, vol. 61, p. 2658, 2007.
- [16] Mattes B I and Kazmerski L I, *Polycrystalline and Amorphous Thin Films and Devices*, Academic Press, 1980.
- [17] Gil A, Colchero J, Gomez-Herrero J and Bar'ó M A, "Electrostatic force gradient signal: resolution enhancement in electrostatic force microscopy and improved Kelvin probe microscopy", *Nanotechnology*, vol. 14, p. 332, 2003.
- [18] Hudlet S, Saint Jean M, Guthmann C, Berger J, "Evaluation of the capacitive force between an atomic force microscopy tip and a metallic surface", *The European Physical Journal B - Condensed Matter and Complex Systems*, vol. 2, p. 5, 1998.
- [19] Argento C and French R H, "Parametric tip model and force–distance relation for Hamaker constant determination from atomic force microscopy", *Journal of Applied Physics*, vol. 80, p. 363680, 1996.
- [20] Toset J, Casuso I, Samitier J and Gomila G, "Deflection-voltage curve modeling in atomic force microscopy and its use in DC electrostatic manipulation of gold

nanoparticles", *Nanotechnology*, vol. 18, p. 015503, 2007.

[21] Hudlet S, Saint Jean M, Guthmann C and Berger J, "Evaluation of the capacitive force between an atomic force microscopy tip and a metallic surface", *The European Physical Journal*, vol. 2, p. 5, 1998.

[22] Hutter J L, "Calibration of atomic-force microscope tips", *Review of Scientific Instruments*, vol. 64, p. 1868, 1993.

[23] Palacios-Lidon E and Colchero J, "Quantitative analysis of tip-sample interaction in non-contact scanning force spectroscopy", *Nanotechnology*, vol. 17, p. 5491, 2006.

[24] Sacha G M and Sáenz J J, "Cantilever effects on electrostatic force gradient microscopy", *Applied Physics Letters*, vol. 85, p. 2610, 2004.

[25] Gomila G, Toset J and Fumagalli L, "Nanoscale capacitance microscopy of thin dielectric films", *Journal of Applied Physics*, vol. 104, p. 024315, 2008.